

INTERSTELLAR TURBULENCE DRIVING BY GALACTIC SPIRAL SHOCKS

CHANG-GOO KIM¹, WOONG-TAE KIM¹, AND EVE C. OSTRIKER²

¹Department of Physics & Astronomy, FPRD, Seoul National University, Seoul 151-742, Republic of Korea and

²Department of Astronomy, University of Maryland, College Park, MD 20742, USA

Draft version July 23, 2018

ABSTRACT

Spiral shocks are potentially a major source of turbulence in the interstellar medium. To address this problem quantitatively, we use numerical simulations to investigate gas flow across spiral arms in vertically stratified, self-gravitating, magnetized models of galactic disks. Our models are isothermal, quasi-axisymmetric, and local in the quasi-radial direction while global in the vertical direction. We find that a stellar spiral potential perturbation promptly induces a spiral shock in the gas flow. For vertically stratified gas disks, the shock front in the radial-vertical plane is in general curved, and never achieves a steady state. This behavior is in sharp contrast to spiral shocks in two-dimensional (thin) disks, which are generally stationary. The non-steady motions in our models include large-amplitude quasi-radial flapping of the shock front. This flapping feeds random gas motions on the scale of the vertical disk thickness, which then cascades to smaller scales. The induced gas velocity dispersion in quasi-steady state exceeds the sonic value for a range of shock strengths, suggesting that spiral shocks are indeed an important generator of turbulence in disk galaxies.

Subject headings: galaxies:ISM — ISM:kinematics and dynamics — turbulence — instabilities — MHD

1. INTRODUCTION

Turbulence in the interstellar medium (ISM) is observed to be pervasive and highly supersonic. Shocks created by random gas motions produce a rich variety of structures in the diffuse, atomic ISM as well as in gravitationally-bound giant molecular clouds (GMCs). Recent work has shown that turbulence is crucial to control of star formation within GMCs, and it is also believed to affect GMC formation processes. Turbulence thus regulates star formation on both local and global scales (e.g., Ballesteros-Paredes et al. 2006). In the absence of driving, shock dissipation and nonlinear cascades cause turbulence to decay on a time scale comparable to flow crossing times even for a medium with equipartition-strength magnetic fields (e.g., Stone, Ostriker, & Gammie 1998; Mac Low 1999; Padoan & Nordlund 1999), amounting to a few tens of Myr for the diffuse ISM. This implies that the ISM must be continuously stirred by one or (likely) more driving sources.

A number of mechanisms have been proposed to drive turbulence, including H II region expansion, supernova explosions, and fluid instabilities involving magnetic fields and gravity (see Mac Low & Klessen 2004; Elmegreen & Scalo 2004 for recent reviews). Although less well recognized, galactic spiral shocks are also an appealing means to generate ISM turbulence. Woodward (1976) showed that cloud deformation by passage of a shock, and the associated Kelvin-Helmholtz instabilities, together trigger random motions in the cloud. Wada & Koda (2004) suggested that an in-plane “wobble instability” of spiral shocks can also drive turbulent motions, although this appears to be suppressed when three-dimensional effects are included (Kim & Ostriker 2006, hereafter Paper I). Very recently, Bonnell et al. (2006) and Dobbs et al. (2006) demonstrated that passage of a distribution of clouds through a spiral shock gives rise to internal turbulent motions that follow Larson’s (1981) empirical scaling law fairly well.

Most of the studies cited above investigate two-dimensional dynamics driven by spiral shocks, neglecting the vertical de-

gree of freedom. When the vertical dimension is taken into account and well-resolved, Paper I showed that non-steady motions of the spiral shock develop.¹ Non-steady behavior of spiral shocks and generation of vertical motions has in fact been seen in previous numerical models by other authors (e.g., Martos & Cox 1998; Gómez & Cox 2002, 2004; Boley & Durisen 2006). In this Letter, we clarify the physical causes of non-stationarity for spiral shocks in stratified disks. We also quantify the level of the induced gas motions to show that vertical spiral shocks should indeed be an important source of turbulence in spiral galaxies.

2. METHODS AND MODEL PARAMETERS

We study evolution of vertically-stratified gas flow across spiral shocks in local regions of self-gravitating, differentially rotating, magnetized galactic disks. Our studies use a modified version of the ZEUS code (Stone & Norman 1992a,b) to solve the time-dependent magnetohydrodynamic (MHD) equations presented in Paper I. We use the same local formulation described in Paper I, which explored fully three-dimensional models. Here, we perform much higher resolution models to focus on the detailed turbulent response, but suppress the degree of freedom parallel to the spiral arm (i.e. our models are quasi-axisymmetric). The reader is referred to Paper I for a complete description of our model prescription and numerical methods. Here, we briefly summarize the coordinate system and model parameters we adopt.

We consider a local region centered on a tightly-wound spiral arm (pitch angle $i \ll 1$), with a potential perturbation due to the stars assumed to be rigidly rotating with pattern speed Ω_p . We introduce a local, co-rotating Cartesian frame centered on $(R, \phi, z) = (R_0, \Omega_p t, 0)$. The local frame is tilted such that $\hat{\mathbf{x}}$ and $\hat{\mathbf{y}}$ denote the in-plane directions perpendicular and parallel, to the arm, respectively, while $\hat{\mathbf{z}}$ is perpendicular to the galactic plane (Roberts 1969). We set up a two-dimensional simulation domain with size $L_x \times L_z$ in the x - z plane (hereafter XZ plane), and assume all physical variables

Electronic address: kimcg@astro.snu.ac.kr, wkim@astro.snu.ac.kr, ostriker@astro.umd.edu

¹The early low-resolution simulations of Tubbs (1980) did not show this effect.

TABLE 1
SUMMARY OF MODEL PARAMETERS AND SIMULATION RESULTS

Model (1)	Q_0 (2)	β_0 (3)	F (4)	Grid (5)	H (pc) (6)	$\langle \sigma_x^2 \rangle^{1/2}/c_s$ (7)	$\langle \sigma_y^2 \rangle^{1/2}/c_s$ (8)	$\langle \sigma_z^2 \rangle^{1/2}/c_s$ (9)	\mathcal{M}_{eff} (10)
A	1.8	∞	5	1024 ²	196	0.66	0.63	0.38	4.0
B	1.8	∞	5	512 ²	196	0.67	0.62	0.36	3.9
C	2.0	∞	7	512 ²	218	1.01	0.86	0.45	5.0
D	2.5	∞	10	512 ²	272	1.55	1.20	0.58	6.2
E	1.5	10	5	512 ²	169	0.64	0.52	0.31	3.8
F	1.8	10	7	512 ²	203	0.93	0.79	0.42	4.4
G	2.0	10	10	512 ²	225	1.54	1.19	0.52	5.4

NOTE. — Col. (1)-(4): Model name and input parameters. Col. (5): Numerical resolution. Col. (6): Vertical scale height of gas in initial magnetohydrostatic equilibrium. Cols. (7)-(9): Density-weighted late-time velocity dispersions. Col. (10): Effective Mach number of the large-scale spiral shock.

to be independent of y . The simulation box size L_x is equal to the arm-to-arm separation. We allow for nonzero values of velocity v_y and magnetic field B_y ; initially $v_y = (\Omega_0 - \Omega_p)R_0 - \Omega_0 x$ and B_y is independent of x , where Ω_0 is the local angular velocity at R_0 . We also include Coriolis forces. This quasi-axisymmetric approximation prevents clump-forming, non-axisymmetric gravitational instabilities from developing, enabling us to focus on the properties of turbulence independent of cloud formation.

We idealize the ISM by treating it as an isothermal gas with effective speed of sound $c_s = 7 \text{ km s}^{-1}$. The initial gaseous disk (without the spiral potential) is in vertical magnetohydrostatic equilibrium. As reference values, we take $R_0 = 10 \text{ kpc}$, $\Omega_0 = 26 \text{ km s}^{-1} \text{ kpc}^{-1}$, and epicyclic frequency $\kappa_0 = 2^{1/2}\Omega_0$ (for a flat rotation curve). The corresponding orbital period is $t_{\text{orb}} \equiv 2\pi/\Omega_0 = 2.4 \times 10^8 \text{ yr}$. For the spiral arm parameters, we adopt $\Omega_p = \Omega_0/2$ and $\sin i = 0.1$. We adopt $L_x = \pi R_0 \sin i = 3.14 \text{ kpc}$ for a two-armed spiral. We impose reflection symmetry with respect to the midplane, and apply open boundary conditions at $z = L_z = 4H$, where H ($\sim 170\text{--}270 \text{ pc}$) is the initial disk scale height. We adopt sheared-periodic boundary conditions in x .

The three key parameters that characterize our model disks are

$$Q_0 = \frac{\kappa_0 c_s}{\pi G \Sigma_0}, \quad \beta_0 = \frac{c_s^2}{v_A^2}, \quad F = \frac{2}{\sin i} \left(\frac{|\Phi_{\text{sp}}|}{R_0^2 \Omega_0^2} \right), \quad (1)$$

where Σ_0 is the gas surface density, v_A is the Alfvén speed, and Φ_{sp} is the amplitude of the imposed sinusoidal potential (Paper I). The quantity F measures the ratio of the perturbed sinusoidal radial force to the mean axisymmetric gravitational force (Roberts 1969). We do not consider the vertical variation of the spiral potential perturbation; the perturbed vertical force is negligible ($< 4\%$) compared to the background vertical force. In our simulations, the potential amplitude slowly increases from 0 to F over $\sim 1.5t_{\text{orb}}$. We present results for seven numerical models, as listed in Table 1.

3. NONLINEAR SIMULATIONS

3.1. Spiral Shock Evolution in a Stratified Disk

In this subsection, we describe the evolution of spiral shocks in our fiducial model G; evolution in other models is similar. As the amplitude of the stellar spiral potential grows, magnetosonic waves emerge and steepen, forming a shock front near $x/L_x = 0.04$ by $t/t_{\text{orb}} \sim 1.0$. At this time, fluid motions are nearly horizontal, and the shock front is nearly vertical. The gravity due to the large post-shock midplane density enhancement soon breaks vertical force balance, however, pulling material at high $|z|$ toward the midplane. With in-

creased postshock density, the shock near $z = 0$ tends to move upstream toward the spiral potential minimum, causing the shock front to bend. Gas entering the curved shock is initially bent upward toward the shock front and then pulled downward due to strong vertical gravity. The falling material establishes repulsive pressure gradients and bounces back to high $|z|$. The instantaneous streamlines shown for model G at $t/t_{\text{orb}} = 1.2$ in Figure 1a reflect gas motions at this stage.

Our model simulations show that spiral shocks in the XZ plane never achieve a steady state, as illustrated by the strong density variations in Figure 1b,c for model G. This result is quite unlike the steady solutions that obtain for models which neglect vertical degrees of freedom (e.g., Woodward 1975; Kim & Ostriker 2002). In particular, when the fluid variables are allowed to vary with z , the gas leaving the right x -boundary does not in general have the same z as it had when it originally entered the left x -boundary², as Figure 1a illustrates. When the vertical gravity exceeds the vertical repulsive pressure force downstream from the shock, post-shock material is drawn toward the midplane, and the shock front at high $|z|$ bends downstream (Fig. 1b). As gas is further compressed, vertical pressure gradients overwhelm vertical gravity and the gas even at $|z|/H \sim 0.5$ is able to rebound to $|z|/H \gtrsim 3$. This in turn forces the shock front at large $|z|$ to shift back upstream (Fig. 1c). The vertically-rebounding gas overshoots equilibrium, vertical gravity again dominates, and the cycle repeats. As gas traverses the spiral arms, therefore, the shocks in our models continue to quasi-periodically shift back and forth perpendicular to the arms. These “flapping” motions of spiral shocks are strongest at high $|z|$. Random motions at scales comparable to the height H are also driven, and many weak shocks develop especially at high $|z|$ (see Fig. 1c).

In addition to large-scale flapping, we find that spiral shocks in model G experience two small-scale instabilities that aid in transfer of random gaseous kinetic energy to smaller scales: an advective-acoustic cycle and vortex generation. The advective-acoustic cycle occurs as the most overdense midplane region perturbs the upstream flows by launching acoustic waves, analogous to the vortical-acoustic cycle for instabilities in isothermal Bondi-Hoyle-Lyttleton accretion (e.g., Foglizzo 2002). Because the spiral shock front is curved in the XZ plane, Crocco’s theorem ensures generation of vorticity. Moreover, strong rising and falling currents of the gas in the post-shock region create a sheared velocity field favorable to Kelvin-Helmholtz instability, which can also gener-

² This is because the fundamental vertical oscillation period need not equal the arm-to-arm flow period, although these timescales are typically within a factor of a few of each other.

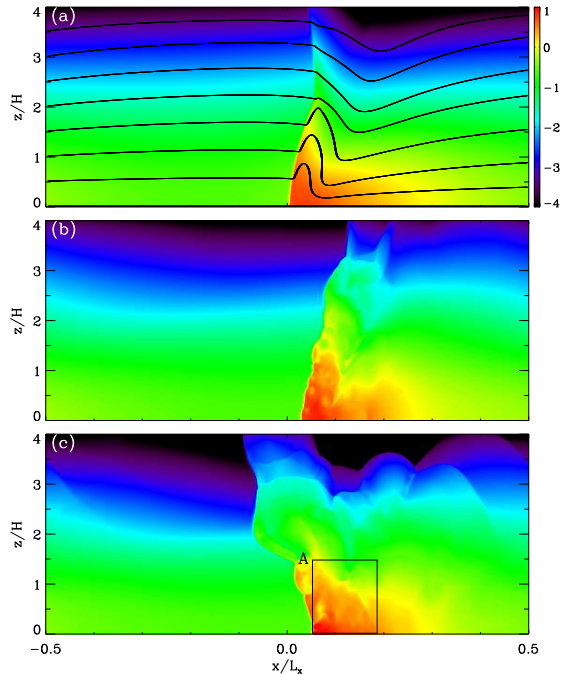


FIG. 1.— Snapshots of density in logarithmic color scale of model G at $t/t_{\text{orb}} = 1.2, 1.7, 1.8$ from top to bottom. Solid lines in (a) represent instantaneous streamlines of gas. The rectangular box A in (c) indicates a sector enclosed in Figure 2.

ate vorticity. We remark that vortices formed at the shock front are not fully resolved in our models because instabilities grow faster at smaller scales. Nevertheless, the velocity dispersions are essentially independent of numerical resolution (see below), suggesting that these instabilities may enhance the small-scale cascade but do not affect the overall level of induced turbulence.

Figure 2 plots typical velocity and density structures inside a spiral arm when turbulence is saturated. Many weak shocks and well-resolved vortices of both signs are apparent. The instantaneous, density-weighted, total velocity dispersion in the region shown in Figure 2 is 1.51 times the sound speed. We find that the power spectra of the perturbed velocities extend smoothly over all scales, indicating fully-developed turbulence. Because of the large-scale shock in v_x , the large shear/streaming in v_y , and the vertical stratification, the power spectrum of v_z as a function of k_x best characterizes the true turbulence. At heights $|z|/H < 1$, this ranges from $v_z^2(k_x) \propto k_x^{-0.5}$ at $n_x \equiv L_x k_x / (2\pi) < 8$ to $v_z^2(k_x) \propto k_x^{-0.8}$ at $8 < n_x < 16$ to $v_z^2(k_x) \propto k_x^{-1.3}$ at $16 < n_x < 64$ for the $k_z = 0$ modes. For $1 < |z|/H < 2$, the power spectra are slightly steeper, having $v_z^2(k_x) \propto k_x^{-0.6}$ at $n_x < 8$, $v_z^2(k_x) \propto k_x^{-1.1}$ at $8 < n_x < 16$, and $v_z^2(k_x) \propto k_x^{-1.7}$ at $16 < n_x < 64$.

3.2. Level of ISM Turbulence

We now quantify the level of random gas motions driven by spiral shocks. Since the velocities in XZ spiral shocks are non-uniform and non-stationary, it is useful to construct the mean velocity field $\langle v_i \rangle$ (with $i = x, y, \text{ or } z$), where the bracket $\langle \rangle$ denotes a time average over $t/t_{\text{orb}} \sim 4-8$ after turbulence saturates. We then measure density-weighted velocity dispersions using $\sigma_i^2 \equiv \int \rho \delta v_i^2 dx dz / \int \rho dx dz$, where $\delta v_i \equiv v_i - \langle v_i \rangle$.³

³ In computing each σ_i , if we initially subtract out velocities corresponding either to unperturbed rotation or to a thin-disk spiral shock (instead of $\langle v_i \rangle$), then the velocity dispersions would be larger.

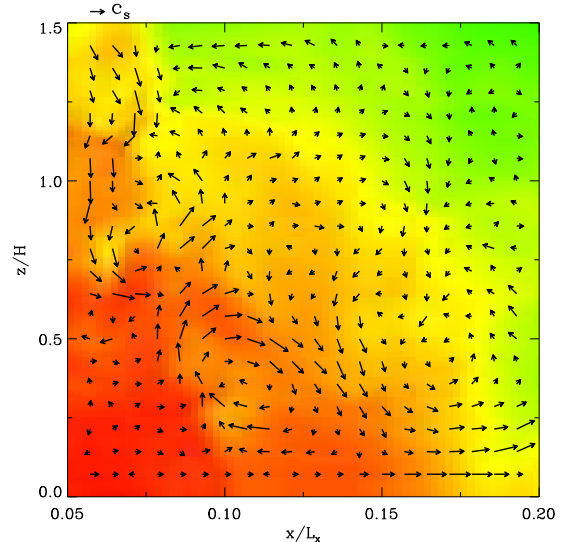


FIG. 2.— Velocity vectors and density in logarithmic scale at $t/t_{\text{orb}} = 3.2$ in the region A marked in Figure 1c. The color scale is the same as in Figure 1. The size of the arrow above the box corresponds to the sound speed.

Figure 3(a) plots $\sigma_i(t)$ for model G, while columns (7)-(9) in Table 1 list $\langle \sigma_i^2 \rangle^{1/2}$ for all the models.

As Figure 3(a) shows, random gas motions in model G are supersonic in the x - and y -directions, and exhibit large-amplitude temporal fluctuations. The characteristic periods of these quasi-periodic fluctuations are in the range $\sim 0.5-0.9 t_{\text{orb}}$. The maximum velocity dispersions occur when the spiral shock is temporarily vertical. Evidently, the system reaches a quasi-steady state in which dissipation of turbulence (in shocks and through cascades) is offset by the continual input of new turbulent energy from the large-scale flapping. Turbulence is strongest in the immediate post-shock region, and declines with increasing distance from the shock. Vertically-averaged velocity dispersions inside the spiral arms typically exceed those in interarm regions by about a factor of 2. For the model parameters we have considered, Table 1 indicates that $\langle \sigma_x \rangle \sim \langle \sigma_y \rangle \sim 2 \langle \sigma_z \rangle$. Comparison of $\langle \sigma_i \rangle$ between models A and B shows that the velocity dispersion is independent of numerical resolution.

What determines the level of velocity dispersions in XZ spiral shocks? Table 1 suggests that stronger shocks (having larger values of Q_0^{-1} , β_0 , and/or F) yield larger σ_i . To characterize the shock strength in each model as simply as possible, we have run one-dimensional counterparts with the same set of parameters, using the thick-disk self-gravity prescription (see Paper I). We define the effective Mach number $\mathcal{M}_{\text{eff}} \equiv \langle \Sigma_2 / \Sigma_1 \rangle^{1/2}$, where Σ_1 and Σ_2 denote the preshock and postshock surface densities, respectively, in the resulting (one-dimensional) spiral shock. Column (10) in Table 1 lists \mathcal{M}_{eff} for each model. Figure 3(b) plots the total velocity dispersion $\sigma_{\text{tot}} = (\langle \sigma_x^2 \rangle + \langle \sigma_y^2 \rangle + \langle \sigma_z^2 \rangle)^{1/2}$ as a function of \mathcal{M}_{eff} . While σ_{tot} monotonically increases roughly as $\sigma_{\text{tot}}/c_s = 0.6 \mathcal{M}_{\text{eff}} - 1.4$ for $\mathcal{M}_{\text{eff}} < 5.5$, it is more or less constant at about $2c_s$ for $\mathcal{M}_{\text{eff}} > 5.5$. We have found that models with other values of Ω_p / Ω_0 follow the same $\sigma_{\text{tot}} - \mathcal{M}_{\text{eff}}$ relation as shown in Figure 3(b).

4. DISCUSSION

Galactic rotation can supply an effectively inexhaustible amount of kinetic energy to power turbulence in the ISM

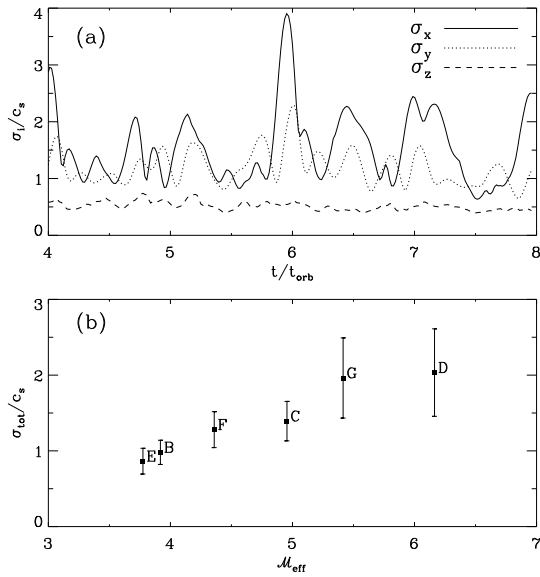


FIG. 3.— (a) Time evolution of the density-weighted velocity dispersions σ_i in model G. (b) Total velocity dispersion σ_{tot} vs. the effective Mach number \mathcal{M}_{eff} of the spiral shock in models B to G. The errorbars represent the standard deviations in the temporal fluctuations of σ_i .

(Fleck 1981).⁴ In this Letter, we have shown that spiral shocks are in general non-stationary in the radial-vertical plane, and can efficiently transform some of the available bulk rotational energy into random gas motions. Vertical force imbalance drives radial flapping of the shock front at $|z|/H \gtrsim 0.2$, which then feeds turbulence at smaller scales. The random gas motions induced by the spiral shock persist despite strong shock dissipation, and yield time-averaged in-plane velocity dispersions $\sim 7-10 \text{ km s}^{-1}$ for a range of shock strengths, similar to the observed line widths of cold and warm atomic gas in the Milky Way (e.g., Heiles & Troland 2003). Vertical velocity dispersions are lower, but still amount to $\sim 1/2$ of the thermal velocity dispersion.

Although our presentation has focused on shocks with realistic parameters, in fact turbulence generation by spiral shocks appears to require neither self-gravity nor magnetic fields. Our model simulations, including those unlisted in Table 1, show that anything (e.g., an imposed variation of Φ_{sp} with

⁴ To maintain a fixed level of turbulence, the energy dissipation per unit mass per unit time must be balanced by the net stresses, $\Omega \langle \rho v_x \delta v_y - B_x B_y / (4\pi) \rangle / \bar{\rho}$ (e.g. Piontek & Ostriker 2005). If this power is supplied at the expense of overall ISM accretion toward the galactic center, the accre-

tion time is $\sim (2\Omega)^{-1} \bar{\rho} (\Omega R)^2 \langle \rho v_x \delta v_y \rangle^{-1}$, which exceeds the Hubble time if $\langle \rho v_x \delta v_y - B_x B_y / (4\pi) \rangle \sim \bar{\rho} c_s^2$.

tion time is $\sim (2\Omega)^{-1} \bar{\rho} (\Omega R)^2 \langle \rho v_x \delta v_y \rangle^{-1}$, which exceeds the Hubble time if $\langle \rho v_x \delta v_y - B_x B_y / (4\pi) \rangle \sim \bar{\rho} c_s^2$. z) that makes the primary shock non-vertical will end up producing a non-steady flow – simply because vertical oscillation periods need not (and in general do not) agree with the horizontal crossing time between arms. Since strong spiral arms usually imply a high rate of star formation, spiral shocks and stellar energy sources may work together in generating turbulence in many galaxies. The absence of observed correlation between spiral arm phase and turbulent amplitude (e.g., Dickey et al. 1990), however, suggests that these two processes are not the only important sources of turbulence. In addition, radio observations of extended HI disks in face-on galaxies show that the total vertical velocity dispersions are as large in the non-star-forming outer parts as in the star-forming inner regions (van Zee & Bryant 1999), again suggesting that additional sources of turbulence are able to compensate when needed.

One compensating source of turbulence may be provided by the magnetorotational instability (MRI) (Sellwood & Balbus 1999; Kim, Ostriker, & Stone 2003; Dziourkevitch et al. 2004). The MRI should naturally be strongest exactly where spiral shocks are absent: in the outer galaxy, where gravity is weak, the disk flares, and the density drops; and in interarm regions, where the angular velocity decreases outward (in arms, shear is reversed so that MRI cannot occur).

While in this Letter we adopt isothermal conditions for the gas and take the mean magnetic field parallel to the spiral arm, the real ISM has a multi-phase structure and is threaded also by weak vertical magnetic fields. Piontek & Ostriker (2004, 2005) demonstrated that MRI is able to generate random gas motions up to $\sim 8 \text{ km s}^{-1}$ in two-phase gas under favorable conditions. It will be interesting to see how turbulent driving in spiral shocks develops for a multiphase medium, and whether MRI and spiral shocks can indeed establish a geographically-compensating balance of power.

We are grateful to S. S. Hong, J. Kim, and D. Ryu for valuable discussions, and to the referee I. Bonnell for a helpful report. This work was supported partly by Korea Science and Engineering Foundation (KOSEF) grant R01-2004-000-10490-0 and partly by NASA under grant NNG05GG43G.

REFERENCES

- Ballesteros-Paredes, J., Klessen, R. S. Mac Low, M.-M., & Vázquez-Semadeni, E. 2006, in *Protostars and Planets V*
- Boley, A. C., & Durisen, R. H. 2006, *ApJ*, 641, 534
- Bonnell, I. A., Dobbs, C. L., Robitaille, T. P., & Pringle, J. E. *MNRAS*, 365, 37
- Dickey, J. M., Hanson, M. M., & Helou, G. 1990, *ApJ*, 352, 522
- Dobbs, C. L., Bonnell, I. A., & Pringle, J. E. 2006, *MNRAS*, submitted; astro-ph/0602103
- Dziourkevitch, N., Elstner, D., Rüdiger, G. 2004, *A&A*, 423, L29
- Elmegreen, B. G., & Scalo, J. 2004, *ARA&A*, 42, 211
- Fleck, R. C. 1981, *ApJ*, 246, L151
- Foglizzo, T. 2002, *A&A*, 392, 353
- Gómez, G. C., & Cox, D. P. 2002, *ApJ*, 580, 235
- Gómez, G. C., & Cox, D. P. 2004, *ApJ*, 615, 744
- Heiles, C., & Troland, T. H. 2003, *ApJ*, 586, 1067
- Kim, W.-T., & Ostriker, E. C. 2002, *ApJ*, 570, 132
- Kim, W.-T., Ostriker, E. C., & Stone, J. M. 2003, *ApJ*, 599, 1157
- Kim, W.-T., & Ostriker, E. C. 2006, *ApJ*, 646, 213 (Paper I)
- Mac Low, M.-M. 1999, *ApJ*, 524, 169
- Mac Low, M.-M., & Klessen, R. S. 2004, *Rev. Mod. Phys.* 76, 125
- Martos, M. A., & Cox, D. P. 1998, *ApJ*, 509, 703
- Padoan, P., & Nordlund, A. 1999, *ApJ*, 526, 279
- Piontek, R. A., & Ostriker, E. C. 2004, *ApJ*, 601, 905
- Piontek, R. A., & Ostriker, E. C. 2005, *ApJ*, 629, 849
- Roberts, W. W. 1969, *ApJ*, 158, 123
- Sellwood, J. A., & Balbus, S. A. 1999, *ApJ*, 511, 660
- Stone, J. M., & Norman, M. L. 1992a, *ApJS*, 80, 753
- Stone, J. M., & Norman, M. L. 1992b, *ApJS*, 80, 791
- Stone, J. M., Ostriker, E. C., & Gammie, C. F. 1998, *ApJ*, 508, L99
- Tubbs, A. D. 1980, *ApJ*, 239, 882
- van Zee, L., & Bryant, J. 1999, *AJ*, 118, 2172
- Wada, K., & Koda, J. 2004, *MNRAS*, 349, 270
- Woodward, P. R. 1975, *ApJ*, 195, 61
- Woodward, P. R. 1976, *ApJ*, 207, 484